nature communications



Article

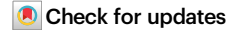
https://doi.org/10.1038/s41467-024-55654-4

Performance and stability analysis of allperovskite tandem photovoltaics in lightdriven electrochemical water splitting

Received: 25 June 2024

Accepted: 19 December 2024

Published online: 02 January 2025



Junke Wang 1,2,6 , Bruno Branco 1,6 , Willemijn H. M. Remmerswaal¹, Shuaifeng Hu 2 , Nick R. M. Schipper 1 , Valerio Zardetto³, Laura Bellini¹, Nicolas Daub¹, Martijn M. Wienk¹, Atsushi Wakamiya 4 , Henry J. Snaith 2 & René A. J. Janssen 1,5

All-perovskite tandem photovoltaics are a potentially cost-effective technology to power chemical fuel production, such as green hydrogen. However, their application is limited by deficits in open-circuit voltage and, more challengingly, poor operational stability of the photovoltaic cell. Here we report a laboratoryscale solar-assisted water-splitting system using an electrochemical flow cell and an all-perovskite tandem solar cell. We begin by treating the perovskite surface with a propane-1,3-diammonium iodide solution that reduces interface non-radiative recombination losses and achieves an open-circuit voltage above 90% of the detailed-balance limit for single-junction solar cells between the bandgap of 1.6–1.8 eV. Specifically, a high open-circuit voltage of 1.35 V and maximum power conversion efficiency of 19.9% are achieved at a 1.77 eV bandgap. This enables monolithic all-perovskite tandem solar cells with a 26.0% power conversion efficiency at 1 cm² area and a pioneering photovoltaicelectrochemical system with a maximum solar-to-hydrogen efficiency of 17.8%. The system retains over 60% of its peak performance after operating for more than 180 h. We find that the performance loss is mainly due to the degradation of the photovoltaic component. We observe severe charge collection losses in the narrow-bandgap sub-cell that can be attributed to the interface degradation between the narrow-bandgap perovskite and the hole-transporting layer. Our study suggests that developing chemically stable absorbers and contact layers is critical for the applications of all-perovskite tandem photovoltaics.

Monolithic tandem solar cells offer the ability to simultaneously possess high photocurrent and photovoltage for converting sunlight into electricity for photovoltaic (PV) power and for direct generation of solar fuels¹. Among the options for tandem solar cells, all-perovskite

double-junction tandem solar cells consisting of wide- (-1.80 eV) and narrow-bandgap (-1.20 eV) perovskite absorbers have demonstrated power conversion efficiencies (PCEs) higher than their single-junction counterparts with sufficient photovoltages to drive water splitting²⁻⁴.

¹Molecular Materials and Nanosystems, Institute of Complex Molecular Systems, Eindhoven University of Technology, partner of Solliance, P.O. Box 513, 5600 MB Eindhoven, The Netherlands. ²Clarendon Laboratory, Department of Physics, Parks Road, Oxford OX1 3PU, UK. ³TNO, partner in Solliance, High Tech Campus 21, 5656 AE Eindhoven, The Netherlands. ⁴Institute for Chemical Research, Kyoto University, Gokasho, Uji, Kyoto 611-0011, Japan. ⁵Dutch Institute for Fundamental Energy Research, De Zaale 20, 5612 AJ Eindhoven, The Netherlands. ⁶These authors contributed equally: Junke Wang, Bruno Branco. e-mail: r.a.j.janssen@tue.nl

In a PV-electrochemical cell (EC) water-splitting system, the operating point is determined by the crossing point between the current density-voltage (J-V) curve of the PV cell and the polarization curve of the EC cell⁵. The solar-to-hydrogen (STH) efficiency is proportional to the device photocurrent and Faradaic efficiency at a sufficient photovoltage (>1.23 V)¹. On the PV side, devices that provide a maximum-power-point voltage (V_{MPP}) that equals or exceeds the operating voltage (V_{OP}) of the EC system will afford high STH conversion. For all-perovskite tandem solar cells, the open-circuit voltage $(V_{\rm OC})$ still lies appreciably below its theoretical limit, which has been mainly attributed to the increased non-radiative recombination occurring at interfaces of the perovskite with charge transport layers^{6,7}. Post-treatments such as using chemical passivation for defect sites, introducing surface dipoles to reduce minority carriers, and increasing physical separation between the perovskite and electron transport layer (ETL) have shown promise in alleviating non-radiative losses at the interfaces⁸⁻¹¹.

The stability of all-perovskite tandem solar cells is another key figure of merit in PV-assisted applications. Extensive prior reports have documented light-induced phase separation and material instability to ambient species as the dominant limiting factors to the stability of single-junction perovskite solar cells, and presented corresponding strategies to mitigate them^{7,12}. However, for integrated all-perovskite tandem solar cells, metal ingression (such as Au) and ion redistribution (such as I⁻) through the interconnecting layer can introduce additional degradation pathways¹³. While long-term maximum-power-point tracking (MPPT) has been the preferred testing protocol for the stability evaluation of complete tandems, few studies have disentangled the degradation events relevant to each sub-cell^{14,15}. Previously, photoluminescence (PL) and electroluminescence (EL) selectively measured from the sub-cells have been utilized to analyze the efficiency potential of tandem solar cells¹⁶. However, it remains challenging to provide a full understanding of the stability-limiting components in a complex tandem device using these techniques.

In this work, we develop a light-driven water-splitting system using efficient all-perovskite tandem solar cells and investigate the related degradation events. To obtain high performance in the tandem device, we sought to suppress non-radiative recombination at the interface between the wide-bandgap perovskite and ETL to reduce energy losses in tandem solar cells. As we reported before11,17-19, we show that post-treatment with a solution of diammonium salts universally improves the perovskite-ETL interface, enabling a $V_{\rm OC}$ above 90% of the detailed-balance limit for singlejunction perovskite solar cells from 1.6 to 1.8 eV bandgaps. This translates to a PCE under AM1.5 G simulated sunlight of 26.0% for allperovskite tandem solar cells at 1 cm² area, coupled with efficient Sn -Pb narrow-bandgap perovskite sub-cells. Additionally, we use the all-perovskite tandem solar cell to directly drive a water splitting electrochemical cell to realize a pioneering PV-EC water-splitting system with a maximum STH efficiency of 17.8%, which retains over 60% of its initial performance for over 180 h. We identify that the drop in STH conversion is mainly due to the degradation of the PV component. Using a dichromatic light-emitting diode (LED) setup, we selectively bias the two sub-cells and analyze the J-V characteristics with and without parasitic transport losses to investigate the limiting component of an integrated tandem device. We observe that the degraded narrow-bandgap sub-cell exhibits significant photocurrent collection losses despite the overall optoelectronic quality of the perovskite absorber remaining unchanged. Combined with crosssectional morphology and chemical analysis, we unveil degradation events originating from the buried interface of narrow-bandgap perovskite and hole transport layer (HTL). Our results highlight that intrinsic material instability pertaining to the narrow-bandgap subcell limits the longevity of all-perovskite tandem solar cells and demands research attention prior to their applications.

Results

Photovoltaic performance of tandem solar cells

To quantify energetic losses at the ETL interface, we measured the quasi-Fermi level splitting (QFLS) using absolute PL²⁰ for a series of perovskite films with varying bandgaps from 1.6 to 1.8 eV in a p-i-n device configuration (Fig. 1a and Supplementary Fig. 1). For pristine perovskite films, deficits were found in the QFLS after depositing an ETL on top and these increased with the bandgap. This suggests increased non-radiative recombination losses at the ETL interface in wider bandgap perovskites. Extended from our previous work^{8,19}, we found that treating the perovskite surface with solution-processed propane-1,3-diammonium iodide (PDAI₂) achieves a virtually lossless ETL interface for both 1.61 and 1.65 eV perovskites and a much-reduced QFLS loss (from 121 to 44 meV) for the 1.77 eV perovskite (Fig. 1b and Supplementary Table 1). We then fabricated 1.61, 1.65, and 1.77 eV single-junction perovskite solar cells (PSCs) in a p-i-n device structure (Methods). Device statistics suggest substantially enhanced $V_{\rm OC}$ and fill factor (FF) values after introducing the PDAI2 surface treatment, leading to a maximum PCE of 23.0%, 22.7%, and 19.9% for 1.61, 1.65, and 1.77 eV single-junction PSCs, respectively (Fig. 1c and Supplementary Fig. 2). Correspondingly, the champion devices achieved a $V_{\rm OC}$ of 1.23, 1.27, and 1.35 V, i.e., above 90% of the detailed-balance limit and among the best-reported values between 1.6 and 1.8 eV bandgaps to date (Supplementary Fig. 3). The best-performing devices exhibit negligible hysteresis and good steady-state power output (Supplementary Fig. 4).

We then fabricated monolithic all-perovskite tandem solar cells comprising 1.77 eV wide-bandgap $Cs_{0.2}FA_{0.8}Pb(I_{0.6}Br_{0.4})_3$ and 1.25 eV narrow-bandgap Cs_{0.05}FA_{0.70}MA_{0.25}Pb_{0.5}Sn_{0.5}I₃ absorbers following a device structure of glass/transparent conductive oxide (TCO)/NiO_x/[4-(3,6-dimethyl-9*H*-carbazol-9-yl)butyl]phosphonic acid (Me-4PACz)/1.77-eV perovskite/[6,6]-phenyl-C₆₁butyric acid methyl ester (PCBM)/PEI (polyethyleneimine)/SnO_x/ Au/poly(3,4-ethylenedioxythiophene):polystyrene (PEDOT:PSS)/ 1.25-eV perovskite/C₆₀/bathocuproine (BCP)/Ag (Fig. 1d, e). On a 1 cm² device area, the tandem developed on commonly used indium tin oxide (ITO) as the front TCO shows a maximum PCE of 24.8% with a $V_{\rm OC}$ of 2.08 V, a FF of 0.81, and a $J_{\rm SC}$ of 14.7 mA cm⁻² (Fig. 1f). The external quantum efficiency (EQE)-integrated J_{SC} values of the 1.77 eV and 1.25 eV sub-cells are 15.6 and 14.4 mA cm⁻², respectively, suggesting that the narrow-bandgap sub-cell limits the J_{SC} (Fig. 1g). This can be mainly attributed to parasitic absorption losses, which reduce the number of photons in the near-infrared (NIR) region that reach the narrow-bandgap sub-cell²¹. Improving the operating current, by definition, is critical to achieving higher STH efficiency¹. We therefore replaced ITO with a NIR-transparent hydrogenated indium oxide (IOH) front contact for tandem cells21. This enables a much-enhanced EQE response from the narrow-bandgap sub-cell and currentmatched J_{SC} in the IOH-based tandem device (~15.7 mA cm⁻²). The champion IOH-based tandem achieved higher PCEs of up to 26.0% on 1-cm² cells, with a J_{SC} of 16.0 mA cm⁻², a V_{OC} of 2.08 V, and a FF of 0.78. The device demonstrates negligible hysteresis, and a statistical summary of performance metrics indicates good reproducibility of tandems built on IOH substrates (Supplementary Figs. 5-6).

To analyze the efficiency potential of all-perovskite tandem solar cells, we determined the intensity-dependent QFLS of wide- and narrow-bandgap sub-cells in the tandem using 455 and 850 nm excitation, respectively, and compared them to identically prepared neat perovskite films on glass substrates (Methods). The pseudo-JV curves of wide-bandgap perovskites suggest a small decrease in $V_{\rm OC}$ (10 mV) upon incorporation in a tandem device, consistent with minimized interfacial losses in the corresponding single-junction (Fig. 1h and Supplementary Table 2). This contrasts with a larger $V_{\rm OC}$ loss (40 mV) registered in the narrow-bandgap sub-cell in the tandem. We note that

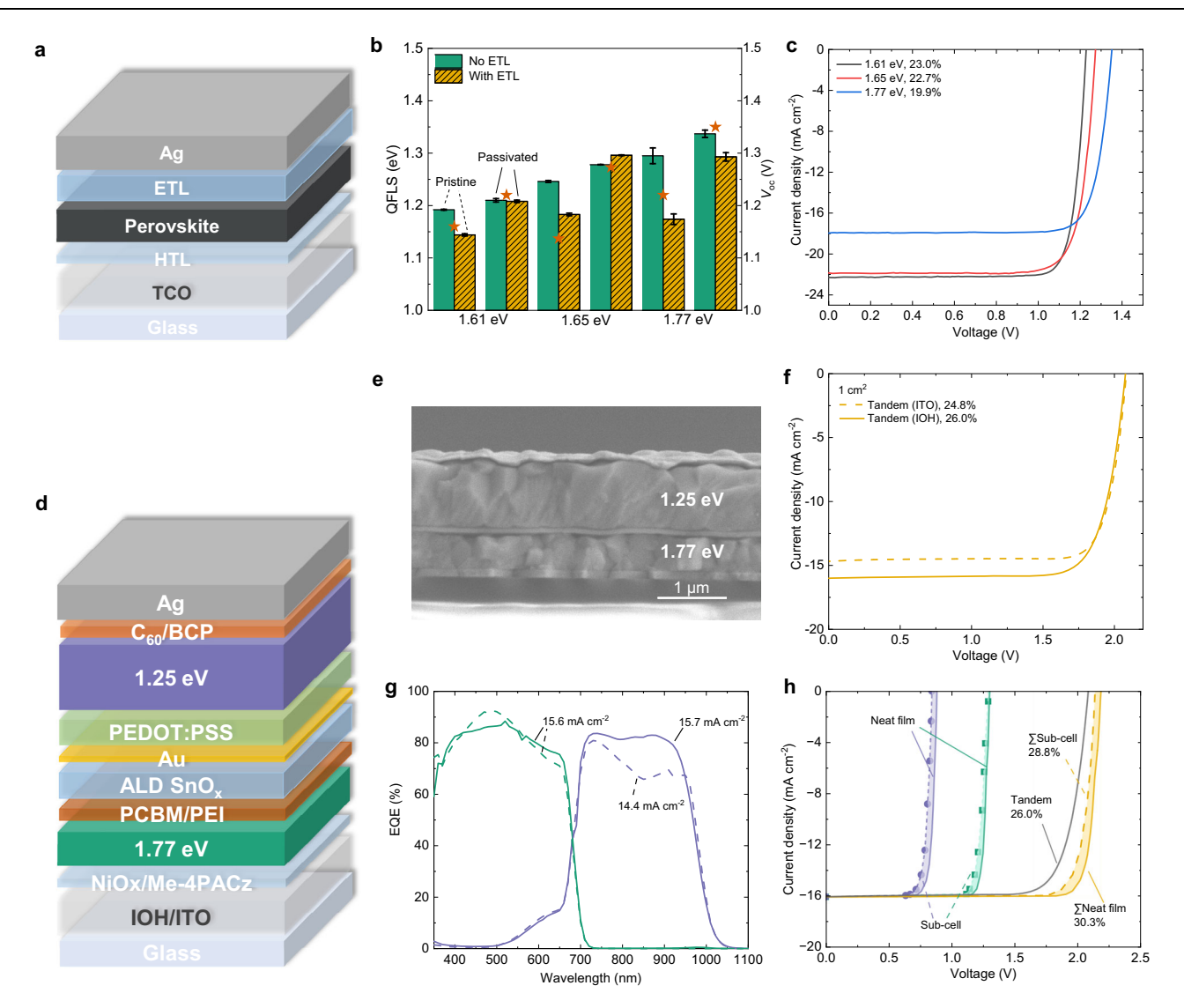


Fig. 1 | **Photovoltaic performance of perovskite solar cells. a** Inverted (p-i-n) device structure of single-junction PSCs. **b** QFLS of 1.61, 1.65, and 1.77 eV perovskite films deposited on TCO/NiO_x/Me-4PACz with (yellow bars) and without ETL (green bars, PCBM or C₆₀, Methods) on top. The stars represent the maximum $V_{\rm OC}$ obtained using each perovskite absorber. **c** J–V curves of the best-performing single-junction PSCs (0.25 cm²). **d** Inverted (p-i-n) tandem solar cell layout, and **e** the corresponding cross-sectional scanning electron microscopy (SEM) image. The scale bar is 1 μm. **f** J–V characteristics of all-perovskite tandem solar cells (1 cm²)

using IOH (solid line) or ITO (dashed line) as the front TCO. **g** EQE spectra of 1.77 and 1.25 eV sub-cells in a double-junction device. The solid lines represent data acquired from IOH and the dashed lines represent those from ITO. **h** Pseudo-JV characteristics of neat films (deposited on glass, solid lines) and sub-cells (in an integrated tandem device, dashed lines) of narrow-bandgap (purple), wide-bandgap (green), and corresponding tandem solar cells (yellow). The J-V curve of the best-performing tandem solar cell (dark solid line) is shown for comparison. Source data are provided as a Source Data file.

this can be attributed to unresolved interface non-radiative recombination and the rough surface on which the narrow-bandgap perovskite is processed on in the tandem^{7,22}. As indicated by the summed pseudo-JV of the sub-cells, suppressing non-radiative recombination at the interconnection layer and minimizing transport losses in the tandem device can improve the device $V_{\rm OC}$ by 50 mV and the FF from 0.78 to 0.84, enabling an efficiency potential of 28.8%²³. Furthermore, after eliminating losses in the transport layers, the PL from the neat perovskite materials suggest an efficiency potential of up to 30.3% for the tandems.

Water splitting with monolithic all-perovskite tandem photovoltaics

The perovskite tandem cell provides a $V_{\rm MPP}$ that exceeds the potential needed for electrochemical water splitting. To demonstrate unassisted water splitting we use a PV-EC system in which the PV and EC parts are

physically separated and wire-connected (Fig. 2a). Integrated photo-electrochemical (PEC) systems have also been demonstrated, where a photoelectrode is used that is externally wired to a second electrode or second photoelectrode. Because metal-halide perovskites are unstable in aqueous electrolytes, these PEC systems use conductive sealants or pastes as a barrier against ingress of the liquid electrolyte and to electrically connect the metal bottom electrode of the PV cell to the electrochemical electrode with the catalyst^{3,24,25}. An advantage of a PV-EC system compared to a PEC is the freedom of design; PV and EC areas can be scaled independently, and there is no need for conductive barriers. The use of two wires for a PV-EC system, as opposed to one for a PEC is not critical in our view. Further, a future PEC system may face difficulties in outdoor operation in case of sub-zero temperatures.

The proton exchange membrane (PEM) water-electrolysis setup is identical to that described previously⁵ and a detailed diagram is shown in Supplementary Fig. 7. The electrolysis cell, with an active area of

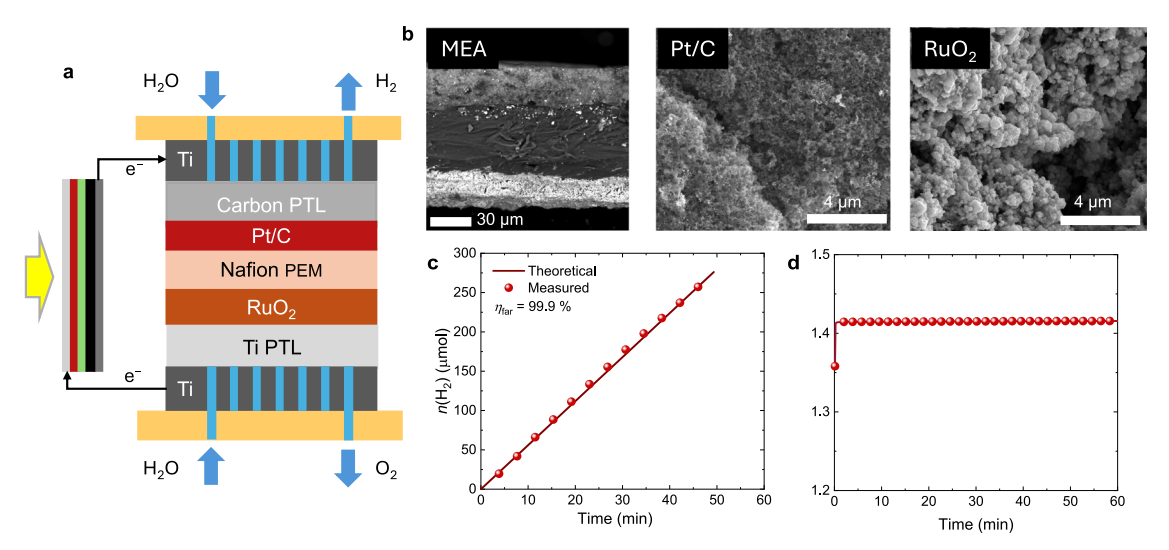


Fig. 2 | **Electrochemical flow cell for light-driven water electrolysis. a** Schematics of the set-up. The electrochemical flow cell comprises a membrane electrode assembly (MEA) consisting of a Nafion® proton exchange membrane (PEM) with Pt/C (HER) and RuO₂ (OER) catalyst layers. Titanium fiber felt and carbon fiber nonwoven fabric are used as porous transport layers (PTL) at the anode and cathode to connect to titanium current collectors with machined parallel flow fields. The electrochemical flow cell is wire-connected to an all-perovskite tandem solar cell.

b Cross-section SEM image of the MEA 5 and top-view SEM images of the Pt/C and RuO $_2$ catalysts on the membrane. **c** H $_2$ evolution vs. time of the electrochemical flow cell measured by gas chromatography in a galvanostatic experiment applying current density of 4.5 mA cm $^{-2}$ during 1 h. **d** Voltage of the electrochemical flow cell vs. time during the galvanostatic measurement. Source data are provided as a Source Data file.

1 cm² (Fig. 2a), was divided into two compartments by a Nafion® PEM coated with 1.2 mg cm⁻² Pt for the hydrogen evolution reaction (HER) and 2.0 mg cm⁻² RuO₂ for the oxygen evolution reaction (OER) on opposite sides. Figure 2b shows scanning electron microscopy (SEM) images of the cross section of a representative catalyst-coated PEM and of the Pt/C and RuO₂ catalysts. The catalyst layers and membrane have a total thickness of roughly 100 µm, allowing higher current densities in comparison to typical batch-type electrochemical cells that are used in light-driven electrochemical water splitting studies. X-ray diffraction (XRD) and X-ray photoelectron spectroscopy (XPS) confirmed the structure and composition of the catalysts (Supplementary Figs. 8 and 9). Millipore purified water ($\rho > 18$ MW cm) was supplied to the electrolysis cell by independent tubing and bottles at room temperature. The Tafel slope of the electrochemical cell was 48.9 mV dec⁻¹ for current densities between 1 and 100 mA cm⁻² (Supplementary Fig. 10), which corresponds to the expected overpotential for the RuO₂ catalyst^{26,27}. Under 1 h galvanostatic operation, the electrochemical cell showed H2 gas evolution with a Faradaic efficiency $(\eta_{\rm far})$ of 99.9% as measured by gas chromatography (Fig. 2c) and a constant V_{OP} of 1.42 V (Fig. 2d).

Next, a monolithic all-perovskite tandem solar cell was used to operate the continuous-flow PEM water electrolysis cell. Rather than encapsulation, which would be appropriate for outdoor applications, we used a nitrogen-filled box to protect the PSC against ambient which enabled full analysis of the cell after prolonged operation. For the integrated system (Fig. 3a, b), the intersection between the polarization curve of the water electrolysis cell and the *J–V* curve of the solar cell determined the operating voltage (1.42 V) and current (14.7 mA) at 1-sun equivalent light intensity (Fig. 3c). Under -1-sun equivalent light intensity the PV-EC system achieved a maximum STH of 17.8% (Fig. 3d) as calculated from:

$$STH = \frac{1.23 I_{OP} \eta_{far}}{A_{sc} P_{in}} \tag{1}$$

where $I_{\rm OP}$ is the operating current (14.5 mA), $\eta_{\rm far}$ is the Faradaic efficiency, $A_{\rm sc}$ is the solar cell area (1 cm²), and $P_{\rm in}$ is the irradiance (100 mW cm⁻²)²⁸. To the best of our knowledge, the obtained STH

represents the highest value for a PV-EC system that uses a monolithic all-perovskite tandem solar cell as the PV component (Supplementary Table 3).

The PV-EC system was operated and monitored continuously under ~1-sun equivalent light intensity for 192 h, after which the experiment was stopped to separately analyze the condition of the operated PV and EC components. During these 192 h, the PV-EC system shows a stable voltage output (Fig. 3d) with a loss of only 10 mV. This results from the steep polarization curve of the water electrolysis cell, such that significant changes in current cause only a small variation in voltage ($I_{EC,1.40V} = 5$ mA and $I_{EC,1.45V} = 50$ mA). Such an operating potential minimizes damage on the electrodes and catalysts, enabling a longer water electrolysis cell lifetime^{29,30}. In contrast, the STH (related to the operating current) is less stable, reaching 90% of the initial value in approximately 52 h and 60% in 184 h. The water electrolysis cell largely retains its original performance in this current range (Fig. 3c). Only at higher current densities a shift of the polarization curve to higher potentials is visible after 192 h of operation. The Tafel slopes, 48.9 vs. 54.8 mV dec⁻¹, indicate a slightly higher kinetic overpotential before and after operation (Supplementary Fig. 10), but its effect is very small in the current density region of interest as the polarization curves virtually overlap. The stability of the electrochemical cell was further investigated by electrochemical impedance spectroscopy (EIS) recorded before and after operation for 192 h (Fig. 3e). The spectra show two semicircles that are associated with the HER (small semicircle at high frequency) and OER (larger semicircle at low frequency)^{31,32}. The spectra were fitted to the equivalent electrical circuit (EEC) depicted in the inset of Fig. 3e where R_{Ω} is the ohmic resistance, Rct is the charge transfer resistance, and CPE is a constant phase element. R_{ct} is related to the kinetic overpotentials that depend on the catalysts and membrane–catalyst interface. Both R_{ct} s drop from 58.9 and 198 Ω cm² to 55.7 and 178 Ω cm² after operation, indicating an improvement of the membrane-catalyst interface. In contrast, the $R_{\rm O}$ increases from 0.132 to 0.148 Ω cm², which led to the shift of the polarization curve at current densities above 100 mA cm⁻² to higher potentials after operation (Fig. 3c). This shows the high stability of the electrochemical cell after operation at low current densities, since the kinetic overpotentials are the determining potentials in operating

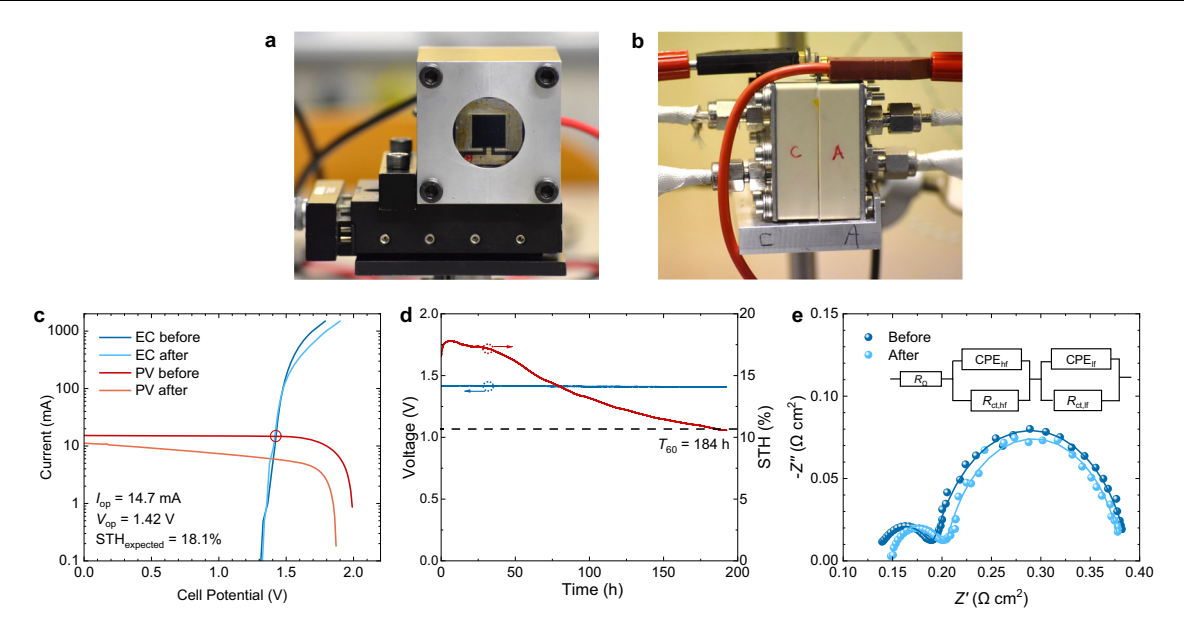


Fig. 3 | **Light-driven water electrolysis. a** Photograph of the all-perovskite $1\,\mathrm{cm}^2$ solar cell in a protective nitrogen-filled box. **b** Photograph of the electrochemical flow cell with temperature-controlled water inlets and outlets on the cathode and anode compartments. The two half-cells are clamped with the Nafion® membrane in the middle. The PV and EC components are wire connected. **c** Intersections of the J-V characteristics of the all-perovskite tandem solar cell measured under simulated AMI.5 G illumination (100 mW cm $^{-2}$) with the polarization curves of the electrochemical flow cell, both before (dark blue and red lines) and after (light blue

and orange lines) 192 h continuous operation. **d** Voltage (blue) and solar-to-hydrogen conversion efficiency (red, STH) vs. time using the integrated PV-EC system during 192 h continuous operation at approx. 1-sun equivalent light intensity. **e** Electrochemical impedance spectroscopy of the electrochemical flow cell before (dark blue) and after (light blue) 192 h continuous operation (solid circles) and fits (solid lines) to the equivalent circuit model shown in the inset. Source data are provided as a Source Data file.

current density range. Further analysis of the Pt/C and ${\rm RuO_2}$ catalysts on the Nafion® membrane with XPS (Supplementary Fig. 11) and XRD (Supplementary Fig. 12) revealed no substantial differences between the membrane-catalyst assembly before and after 190 h of operation. Hence, the drop in STH for the PV-EC system is mainly associated with the degradation of the all-perovskite tandem solar cell.

In our study, using Pt/C and RuO₂ catalysts, the $V_{\rm OP}$ (1.42 V) is significantly lower than the $V_{\rm MPP}$ (1.59 V) of the tandem solar cell (Fig. 3c). Hence, all-perovskite tandem cells offer interesting perspectives for use with earth-abundant (mostly Ni-based) OER and HER catalysts, which typically have a higher $V_{\rm OP}$ in the range of 1.48 to 1.52 V^{33–36}. Importantly, this would lead to only a slight decrease in STH efficiencies (Supplementary Fig. 13). Even when $V_{\rm OP} = V_{\rm MPP}$, the STH would still be 17.3%. In this context, all-perovskite tandems cells ($V_{\rm OC} = 2.1$ V) provide a better application perspective in combination with earth-abundant catalysts than perovskite-silicon tandems cells, where $V_{\rm MPP}$ and $V_{\rm OC}$ (1.7–1.9 V, Supplementary Table 3) are typically lower—especially under conditions where the light intensity is less than 1 sun—a decreased $V_{\rm MPP}$ under $V_{\rm OP}$ would cause a significant loss in the STH.

Degradation events of the PV component

Understanding the degradation mechanism of monolithic all-perovskite tandem solar cells remains challenging, as conventional *J–V* and MPPT measurements provide limited information on the electronic properties of individual components connected in series^{16,37,38}. We first compared the EQE spectra of tandem devices before and after aging (Fig. 4a). In the normalized EQE spectra, we found that the wide-bandgap sub-cell exhibits a slightly redshifted PV onset after the operation (52 meV, Supplementary Fig. 14), a phenomenon previously attributed to light-induced halide segregation in wide-bandgap mixed-halide perovskites^{39–41}. Additionally, Lin et al. have observed a similar redshift in absorption and spectral response of wide-bandgap mixed-halide perovskites during aging, and correlated this with the growth of bromide-rich impurity phases, as part of the

degradation product⁴². It is also possible that the same mechanism is occurring in our wide-gap cells here. The EQE-integrated J_{SC} slightly increases from 15.6 to 16.4 mA cm⁻², suggesting that the current extraction in the wide bandgap is unhampered, despite the compositional change (Supplementary Figs. 14 and 15). In contrast, the J_{SC} of the aged narrow-bandgap sub-cell is drastically reduced from 15.3 to 7.9 mA cm⁻², but the overall shape of the normalized EQE curve remains unchanged. This points to a large reduction of charge collection efficiency from the sub-cell and suggests that structural changes in the bulk of the narrow-bandgap perovskite remain insignificant after aging⁴³.

We examined the cross-sectional morphology of degraded tandem devices using SEM and found large voids near the bottom interface of the narrow-bandgap perovskite sub-cell after aging (Fig. 4b). This has been attributed to the decomposition of narrow-bandgap perovskites in contact with PEDOT:PSS layer, which forms iodine species and further oxidizes Sn²⁺ to Sn⁴⁺ under the stimulus of light or heat⁴⁴. To verify the degradation effect of different HTLs, we compared narrow-bandgap films processed on PEDOT:PSS with films on poly(triaryl amine) (PTAA), bare ITO, and [2-(3,6-dimethoxy-9H-carbazol-9yl)ethyl]phosphonic acid (MeO-2PACz), which have been previously used as HTLs for narrow-bandgap PSCs^{21,43,45}. After post-annealing at 85 °C for 4 h in the dark, pinholes were also formed at the PEDOT:PSS interface and resulted in a morphology similar to the tandem device after 200 h of operation under 1 sun illumination (Fig. 4c). In comparison, no significant changes were recorded for other samples after aging the films for up to 48 h (Fig. 4d-f and Supplementary Fig. 16). This suggests that PEDOT:PSS material could accelerate the decomposition of narrow-bandgap perovskites, while the rest of the examined materials show less damage. Additionally, XRD patterns show no noticeable structural changes after annealing at 85 °C for 24 h, suggesting that the loss in charge collection efficiency can mainly originate from the interface between the narrow-bandgap perovskite and PEDOT:PSS HTL (Fig. 4g).

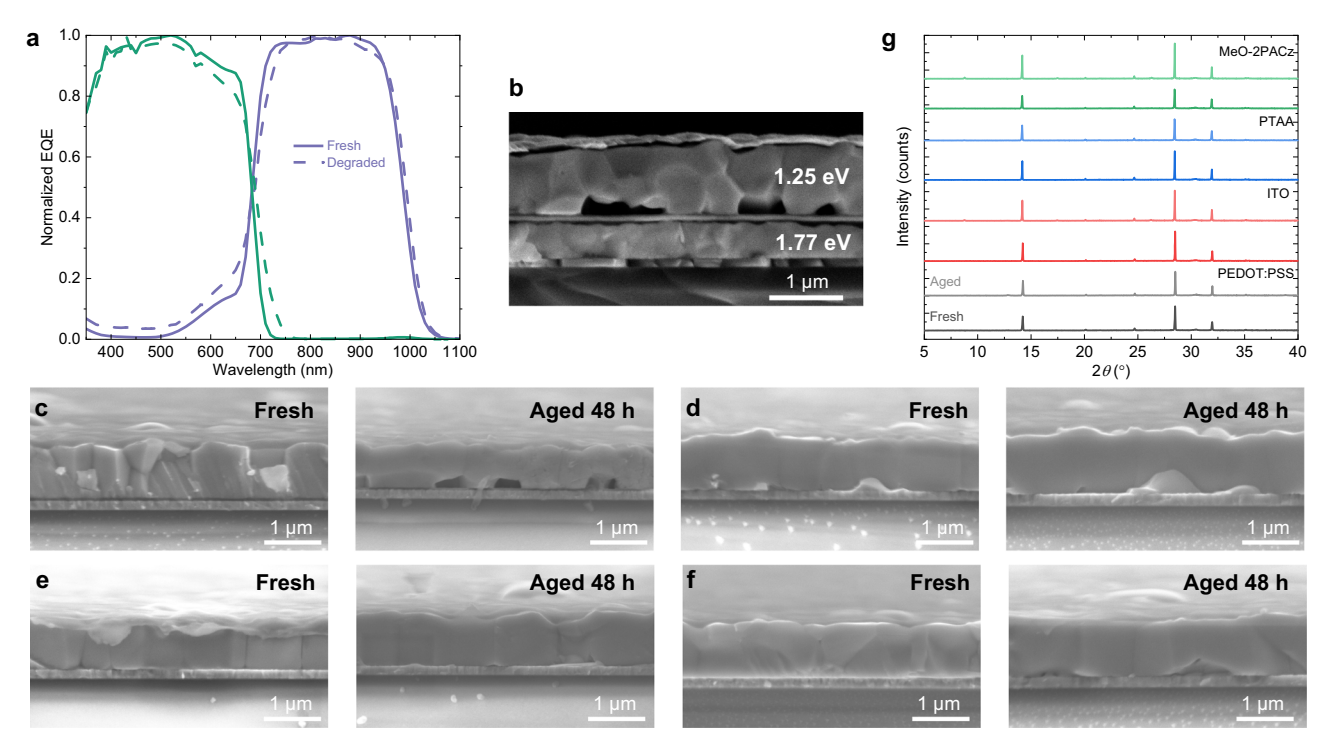


Fig. 4 | **Characteristics of aged perovskite sub-cells. a** Normalized EQE spectra of wide- (green) and narrow-bandgap (purple) sub-cells before (solid lines) and after (dashed lines) aging. **b** Cross-sectional morphology of an aged all-perovskite tandem solar cell after the PV-EC experiment. Cross-sectional morphology of narrow-

bandgap perovskite films deposited on (c) PEDOT:PSS, (d) PTAA, (e) bare ITO, and (f) MeO-2PACz before (left) and after (right) aging at 85 °C in the dark. All scale bars are 1 μ m. g XRD patterns of narrow-bandgap perovskite films aged for 24 h at 85 °C in the dark on different HTLs. Source data are provided as a Source Data file.

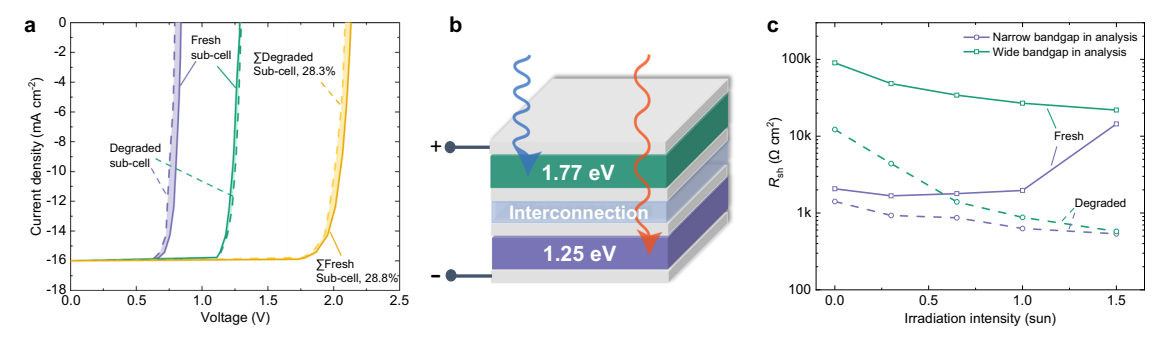


Fig. 5 | **Degradation analysis for all-perovskite tandem solar cells.** a Pseudo-JV characteristics of narrow- (purple) and wide-bandgap (green) sub-cells and reconstructed tandem solar cells (yellow), before (solid lines) and after (dashed lines) degradation. The J_{SC} is shifted to 16.0 mA cm⁻² for comparison. **b** Schematics of sub-cell J-V analysis using a dichromatic LED setup. **c** R_{sh} of tandem solar cells

determined from the J-V curves measured under different biasing conditions. The sub-cell in analysis was measured from 0 to 1.5 sun equivalent illumination intensities while keeping the other sub-cell overbiased (1.7 and 1.5 sun for the narrow-and wide-bandgap, respectively). Source data are provided as a Source Data file.

We proceeded to analyze the impact of degradation in the narrow-bandgap sub-cell on device performance using the intensity-dependent QLFS (Fig. 5a). Compared to the wide-bandgap sub-cell, the narrow-bandgap perovskite exhibits a slightly larger drop in the implied $V_{\rm OC}$, indicating increased non-radiative recombination losses in the sub-cell (Supplementary Table 4). Notably, the pseudo-FF values of both sub-cells remain almost unchanged, leading to a resistance-free pseudo-PCE of 28.3% for a degraded tandem device. This value is very close to that obtained from the fresh tandem device (28.8%). Hence, the large drop in current output after aging suggests that the degraded cell suffers from severe transport losses, likely caused by the high density of voids formed at the buried interface of the narrow-bandgap sub-cell.

To disentangle loss contributions from either sub-cell, we performed sub-cell J–V analysis using a dichromatic LED setup (Fig. 5b and Supplementary Fig. 17) 37 . Single green (530 nm) and infrared (940 nm) LEDs were used to bias the wide-bandgap and narrow-bandgap subcells, respectively. For a fresh tandem, we first determined the shunt resistance ($R_{\rm sh}$) under conditions where we light-bias either the narrow- or wide-bandgap sub-cell (940 nm at 1.7 suns and 530 nm at 1.5 suns, respectively) (Fig. 5c). The $R_{\rm sh}$ is 90 k Ω cm 2 when only biasing the narrow-bandgap sub-cell (wide-bandgap limited) and 2 k Ω cm 2 when only biasing the wide-bandgap sub-cell (narrow-bandgap limited). When the narrow-bandgap sub-cell gradually ceases to be current-limiting by applying excitation also at 940 nm, $R_{\rm sh}$ increases to above 14 k Ω cm 2 approaching the value when the wide-bandgap

sub-cell is limiting³⁷ (Fig. 5c and Supplementary Table 5). For the degraded tandem, the initial $R_{\rm sh}$ decreased to 1.4 k Ω cm² under narrowbandgap sub-cell limited conditions. Interestingly, in this case, simultaneous illumination of the narrow-bandgap sub-cell (940 nm up to 1.5 suns) does not improve the $R_{\rm sh}$ but causes a further reduction of $R_{\rm sh}$ to about $0.5 \,\mathrm{k}\Omega\,\mathrm{cm}^2$. For the degraded tandem, the R_{sh} measured under wide-bandgap sub-cell limited conditions is 12 kΩ cm², i.e., also lower than for the fresh cell. Simultaneous illumination at 530 nm further reduces $R_{\rm sh}$, also to about $0.5 \,\mathrm{k}\Omega\,\mathrm{cm}^2$. This demonstrates that $R_{\rm sh}$ of the degraded tandem is determined by the $R_{\rm sh}$ of the narrow-bandgap subcell. The cause for the low $R_{\rm sh}$ of the narrow-bandgap sub-cell might be the presence of real shunt pathways, but as we show below a possibly more likely explanation is that the photocurrent has become electricfield dependent as a consequence of the micrometer-sized voids present at the interface of the narrow-bandgap perovskite with the PED-OT:PSS layer that hamper photocurrent collection. Such apparent photo-shunts indicate poor charge-carrier extraction⁴⁶.

Besides the intrinsic material stability, metal (Au) diffusion and ion (I⁻/Br⁻) migration through the interconnecting layer have also raised concerns about the device stability of monolithic all-perovskite tandem solar cells¹³. To investigate other factors that may contribute to a low R_{sh} , we recorded XPS depth profiles and found no compelling differences in the atomic concentrations between the fresh and degraded tandem devices (Supplementary Fig. 18). The concentration of oxygen atoms remains very low (≤1%) until reaching the narrowbandgap perovskite/PEDOT:PSS/Au/SnO_x interface. This indicates that environmental oxygen is not the major source of degradation in the narrow-bandgap sub-cell⁴⁵. Additionally, after aging, the tandem device mostly retained its structural integrity, with little evidence of Au or Br diffusion from underlying layers into the narrow-bandgap perovskite absorber. This indicates that the thin contact layers processed by atomic-layer-deposition (ALD) and sputtering techniques can delay device degradation. It also supports our view that the low $R_{\rm sh}$ measured under illumination mainly results from a field-dependent photocurrent caused by the voids and delamination found at the interface between the narrow-bandgap perovskite and the PEDOT:PSS layer of the recombination contact (Fig. 4b). Importantly, we note that we cannot exclude the possibility of I⁻ migration from the rear Sn-Pb perovskite into the front wide-gap perovskite absorber, red shifting the spectral response of the wide-bandgap sub-cell as discussed above. This is due to the limitation of the XPS depth profile technique (see discussions in Supplementary Fig. 18) and further investigations are thus of interest. Despite that, our sub-cell analysis suggests that the wide-bandgap under study is not limiting the tandem performance and future research should focus on the stability related to the narrowbandgap perovskites.

We discuss here that intrinsic material instability remains a major limiting factor for narrow-bandgap sub-cells and complete all-perovskite tandem solar cells. While degradations imposed by exogenous oxidants can be mitigated using robust passivation and encapsulation techniques, improving the intrinsic stability of narrow-bandgap sub-cells is a pressing issue that necessitates further investigations of chemically stable absorbers and charge transport layers⁷. Our accelerated aging tests suggest that other HTLs such as MeO-2PACz can suppress the degradation of narrow-bandgap perovskites, however, compatible tandem device structures are yet to be established to accommodate contact materials with high performance and reproducibility^{21,22}.

Discussion

We reported methods to suppress energetic and optical losses in allperovskite tandem solar cells and achieved efficiencies of up to 26.0% efficiency at a 1 cm² active area. A solar-driven water electrolysis system, consisting of a tandem solar cell and a water electrolysis cell, achieved a maximum STH conversion efficiency of 17.8% and maintained over 60% of its initial performance for 184 h. We have identified that degradation of the narrow-bandgap Sn-Pb perovskite sub-cell in the PV component was primarily responsible for the performance loss. We have found that the narrow-gap sub-cell exhibits a field-dependent photocurrent collection after device degradation caused by delamination and formation of micrometer-sized voids near the recombination contact.

As shown in Supplementary Table 3, very limited studies have used monolithic all-perovskite tandem solar cells for water splitting, with a few showing system stabilities over 100 h. We produced a PV-EC system that exhibits a high STH conversion and operational stability relevant for future development. We presented comprehensive subcell characterization to help analyze the limiting component of integrated tandem devices. We expect that most recent surface modifiers and contact layers suppressing the degradation of Sn-Pb perovskites can simultaneously improve the stability of all-perovskite tandem solar cells and the corresponding PV-EC system^{47,48}. Next to the development of the PV device, designing earth-abundant catalysts with low operating voltages is required to improve the cost effectiveness of the EC system.

Methods

Material and precursor preparation

All materials were used as received without further purification, unless stated otherwise. Patterned glass/ITO substrates were purchased from Naranjo Substrates. CsI (99.99%), SnI $_2$ (99.99%), guanidine thiocyanate (GuaSCN, 99%), glycine hydrochloride (99%), SnF $_2$ (99.99%), PEI solution (M_n ~ 60,000 g mol $^{-1}$, 50 wt% in H $_2$ O), and all anhydrous solvents were purchased from Sigma-Aldrich. PbI $_2$ (>98%), PbBr $_2$ (>98%), Me4PACz (>99.0%), and MeO-2PACz (>98.0%) were purchased from TCI Chemicals. Formamidinium iodide (FAI), methylammonium iodide (MAI), PDAI $_2$, and ethane-1,2-diammonium iodide (EDAI $_2$) were purchased from Greatcell Solar Materials. PCBM was purchased from Nano-C, C $_{60}$ (99.95%) was purchased from SERS Research, and BCP (99.5%) was purchased from Lumtec. PEDOT:PSS (Al4083) was purchased from Heraeus Clevios. NiO $_x$ nanoparticles (2.5 wt% dispersed in ethanol) were purchased from Avantama. PTAA (M_w ~ 56 kDa, PDI 2.87) was purchased from Ossila.

1.77 eV perovskite (Cs_{0.2}FA_{0.8}Pb(I_{0.6}Br_{0.4})₃) precursor solution was prepared by dissolving 1.2 M CsI (0.2), PbBr₂ (0.6), PbI₂ (0.4), and FAI (0.8) in N,N-dimethylformamide (DMF) and dimethyl sulfoxide (DMSO) at a volume ratio of 4:1. 1.65 eV perovskite (Cs_{0.1}FA_{0.9}Pb(I_{0.77}Br_{0.23})₃) precursor solution was prepared by dissolving 1.5 M CsI (0.1), PbBr₂ (0.345), PbI₂ (0.655), and FAI (0.9) in DMF and DMSO at a volume ratio of 4:1. 1.61 eV perovskite (Cs_{0.1}FA_{0.9}Pb(I_{0.85}Br_{0.15})₃) precursor solution was prepared by dissolving 1.5 M CsI (0.1), PbBr₂ (0.225), PbI₂ (0.775), and FAI (0.9) in DMF and DMSO at a volume ratio of 4:1. Narrowbandgap perovskite precursor solution (Cs_{0.05}FA_{0.70}MA_{0.25}Pb_{0.5}Sn_{0.5}I₃) was prepared by dissolving 1.8 M CsI (0.05), MAI (0.25), PbI₂ (0.5), SnI₂ (0.5), FAI (0.7), SnF₂ (0.05) in DMF and DMSO at a volume ratio of 4:1. Additionally, 4 mg guanidine thiocyanate⁴⁹ and glycine hydrochloride¹¹, and 5 mg Sn powder⁵⁰ were added into 1 mL precursor solution. All perovskite solutions were dissolved at 60 °C for 1 h and filtered by 0.22 um PTFE syringe filter before use.

NiO $_x$ solution was prepared by diluting 2.5 wt% NiO $_x$ in ethanol at a volume ratio of 1:10. Me-4PACz was prepared by vortexing the solution in ethanol at a concentration of 0.3 mg mL $^{-1}$ for 1 min. PCBM was prepared by dissolving the material in chlorobenzene (CB) at a concentration of 15 mg mL $^{-1}$ at 60 °C for 1 h. PEI solution was prepared by diluting in 2-propanol at a concentration of 0.025 wt%. PEDOT:PSS was prepared by diluting in 2-propanol at a volume ratio of 1:2. PDAI $_2$ was prepared by dissolving it in 2-propanol/CB (2:1, v/v) solvent at a concentration of 0.5 mg mL $^{-1}$. EDAI $_2$ was dissolved in 2-propanol/toluene (4:3, v/v) solvent at a concentration of 0.5 mg mL $^{-1}$.

Single-junction solar cell preparation

For wide-bandgap single-junction solar cells, NiO_x nanoparticle solution was spin coated on cleaned FTO substrates ($10 \Omega \text{ sq}^{-1}$, AGC Inc.) at 3000 rpm for 30 s (1000 rpm s^{-1}) in air without any post-treatment. The substrates were transferred into a N_2 -filled glovebox, where Me4PACz was spin coated at 3000 rpm for 30 s (1000 rpm s^{-1}) and annealed at 100 °C for 10 min. Then the wide-bandgap precursor (1.61, 1.65, 1.77 eV) was spin coated on top at $1000 \text{ rpm for } 10 \text{ s } (500 \text{ rpm s}^{-1})$ and $5000 \text{ rpm for } 30 \text{ s } (2500 \text{ rpm s}^{-1})$. A 150 µL antisolvent anisole was dropped onto the spinning substrate at 5 s before the end. The substrate was then annealed at 100 °C for 15 min. After cooling, PDAI $_2$ was spin coated dynamically at $4000 \text{ rpm for } 30 \text{ s } (2000 \text{ rpm s}^{-1})$ and annealed at 100 °C for 5 min. PCBM was then spin coated at $1000 \text{ rpm for } 30 \text{ s } (1000 \text{ rpm s}^{-1})$ and followed by evaporating 8 nm BCP and 140 nm Ag on top by thermal evaporation.

For narrow-bandgap single-junction solar cells, PEDOT:PSS was spin coated on cleaned substrates at 4000 rpm for 30 s (1000 rpm s $^{-1}$) and annealed at 160 °C for 15 min. The substrates were then transferred into a N_2 -filled glovebox, where the narrow-bandgap precursor was spin coated at 1000 rpm for 10 s (200 rpm s $^{-1}$) and 3800 rpm for 45 s (1000 rpm s $^{-1}$). A 300 μL antisolvent CB was dropped onto the spinning substrate at 18 s before the end. The substrate was then annealed at 100 °C for 10 min. After cooling, EDAl $_2$ was spin coated at 4000 rpm for 25 s (1300 rpm s $^{-1}$) and annealed at 100 °C for 5 min. 20 nm C_{60} , 8 nm BCP, and 140 nm Ag layers were sequentially deposited on top by thermal evaporation.

For the aging tests, narrow-bandgap perovskite films were deposited on the top of PEDOT:PSS, MeO-2PACz, PTAA, or bare glass/ITO substrates to mimic the growth conditions in full devices, and covered with a thin film of spin-coated PMMA. All films were encapsulated with a cover glass and UV-cured adhesive (Eversolar AB-341, Everlight Chemical Industrial Co.) which was cured under a UV lamp (365 nm) for 3 min inside a N₂-filled glovebox before aging under 85 °C in the dark or under 85 °C under simulated 1-sun illumination.

Monolithic tandem solar cell fabrication

For tandem solar cells, the preparation procedure for corresponding single-junction sub-cells is stated above. For the interconnecting layer, after depositing PCBM on top of the wide-bandgap absorber, a PEI solution was spin coated at 4000 rpm for 30 s (2000 rpm s⁻¹) without any post-treatment. The substrates were then transferred to a homemade spatial ALD reactor to deposit 45 nm $\rm SnO_{xv}$, as described previously^{S1}. The substrates were then transferred back to a thermal evaporator to deposit 1 nm Au and followed by depositing PEDOT:PSS layer in the air and thermal annealing at 120 °C, before depositing the narrow-bandgap sub-cell.

Solar cell characterization

For single-junction solar cells, J-V measurements were performed in ambient air without encapsulation at room temperature, under simulated AM1.5 G irradiance generated by a Wavelabs SINUS-220 solar simulator) calibrated with a certified KG3-filtered reference Si diode (Fraunhofer). A black shadow mask with an aperture area of 0.25 cm² was used. A Keithley 2400 source meter was used to sweep the voltage from forward bias to short-circuit in a reverse scan and from shortcircuit to forward bias in a forward scan, with a scan rate of 0.3 V s⁻¹. Active MPP tracking measurements using a gradient ascent algorithm were performed for 30 s to obtain the steady-state power conversion efficiency. For tandem solar cells, a calibrated tungsten-halogen lamp was used to simulate the solar spectrum (~100 mW cm⁻²), and shadow masks were used to define the illumination area (1 cm^2) . The J-Vmeasurements were performed in a N₂-filled glovebox at a scan rate of 0.25 V s⁻¹. For the EQE measurements, a modulated tungsten-halogen lamp was used as the light source. The signal of solar cells was amplified by a current preamplifier (Stanford Research, SR 570) and measured by a lock-in amplifier (Stanford Research, SR 830). The spectral response was transformed into EQE using a calibrated silicon reference cell. For tandem solar cells, a 940-nm LED bias was used to measure the response from the 1.77 eV front sub-cell and a 530-nm LED bias was used to measure the response from the 1.25 eV back sub-cell.

Sub-cell J-V analysis

The sub-cell J-V analysis was performed at the EQE setup, where two LEDs with 530 and 940 nm wavelengths were used to illuminate tandem solar cells through an aperture of $0.0314~\rm cm^2$ to ensure a high homogeneity. Similar to a previously reported method³⁷, EQE spectra were first acquired to calculate the $J_{\rm SC}$ of both sub-cells. The irradiation intensity for the sub-cell in-analysis was determined by measuring the $J_{\rm SC}$ of the tandem while the other sub-cell was highly biased by another LED (> 1.5 suns). A Keithley 2400 source meter was used to sweep the voltage from +2.2 V to -0.1 V at a scan rate of 0.25 V s⁻¹ in a reverse scan. The $R_{\rm sh}$ was determined from the slope of J-V curves near the short-circuit.

Materials and membrane-electrode assembly preparation

NafionTM membrane NRE-212 was purchased from Ion Power. Pt/C (40 wt%) was purchased from Sigma Aldrich. RuO₂ (anhydrous, 99.9%) and Nafion dispersion (D-521) were purchased from Alfa Aesar. RuO₂ was stored inside an inert atmosphere. 2–propanol was purchased from Biosolve. All catalyst inks were prepared using water purified in the Millipore system (ρ > 18 M Ω cm).

The catalyst inks consisted of 5 wt% solid content, with a 3:1 ratio of catalyst to Nafion ionomer in a 2-propanol: H_2O (4:1) mixture. In the RuO2 ink, Nafion dispersion was first added to catalyst powder, followed by 2-propanol: H_2O . In the Pt/C ink, the catalyst powder was first mixed with water to avoid combustion of the carbon particles, and afterwards, the Nafion dispersion and 2-propanol were consecutively added. The inks were ultrasonicated for at least 10 min prior to catalyst deposition. The catalyst inks were manually spray-coated using a pneumatic airbrush (Aerotec) through a stainless-steel mask with a 2 × 2 cm² opening on opposite sides of the membrane until the target loadings of 1 and 2 mg cm² for Pt and RuO2 were reached, respectively. The catalyst loadings were calculated by weighing the membrane before and after the spray-coating process. The deposition was done at 85 °C to evaporate the solvent immediately upon deposition and to avoid excessive membrane swelling.

Proton exchange membrane electrochemical cell setup

Water electrolysis tests were carried out in an in-house built PEM water electrolysis cell $(5 \times 5 \text{ cm}^2)$ using high-impact polypropylene (PP) as end plates and titanium current collectors (1 mm thick) with machined parallel flow fields (1 mm wide, channel area: 2.25 × 2.25 cm²). Titanium fiber felt $(2.5 \times 2.5 \text{ cm}^2, 0.2-0.3 \text{ mm}, \text{ porosity: } 53-56\%, \text{ from Fuel Cell}$ store) and carbon fiber non-woven fabric ($2.5 \times 2.5 \text{ cm}^2$, $255 \mu\text{m}$, with MPL, H23 C2, from Quintech) were used as PTL at the anode and cathode, respectively. The MEA was pressed between the PTLs and the electrolyzer was sealed with PTFE (5 × 5 cm², 200 μm, from Polyfluor) and closed using a torque of 0.8 Nm. Polyimide film (50 µm, from Wu Xi Shun Xuan New Materials Co., Ltd) was used between the Ti PTL and the membrane to delimit the active area to 1 cm². Millipore purified water ($\rho > 18 \text{ M}\Omega$ cm) was circulated using a peristaltic pump (Masterflex® L/S® Digital Miniflex®) into both anodic and cathodic compartment at 10 mL min⁻¹. Independent water lines and feeding bottles were used for each compartment. The water bottles were bubbled with nitrogen to prevent oxygen and hydrogen build-up.

Electrochemical characterization

Galvanostatic polarization curves were measured using a 2-channel Keithley 2600 SMU controlled by LabVIEW. The first channel was used to apply the current whereas the second channel was used to measure

the voltage across the PEM electrochemical cell. EIS was performed using a potentiostat PGSTAT30 (Autolab) equipped with a frequency analyzer (FRA) module. Water was circulated through the cell for 1 h to allow membrane swelling and equilibration prior to any measurements. The cell was first conditioned by applying 10, 20, 50 and 100 mA cm⁻² for 30 s and then 250 mA cm⁻² for 30 min. The galvanostatic polarization curve was recorded from 0.01 to 375 mA cm⁻². Each current density step was held for 2 min to allow voltage stabilization and the average of the last 10 s was taken as the voltage value. All measurements were performed at room temperature.

Hydrogen evolution

 $\rm H_2$ evolution was measured using a compact gas chromatograph CGC 4.0 (Global Analyzer Solutions-Interscience B.V.) controlled by Chromeleon 7 software (Thermo Fischer Scientific). An EL-FLOW Prestige mass flow controller (Bronkhorst Nederland) was used to control the nitrogen flow ($F_{\rm N2}$ = 135 mL min⁻¹) through the cathode water feeding bottle and the outlet was connected to the CGC 4.0. Once every 3.8 min a sample was taken into the gas chromatograph for analysis. A thermal conductivity detector was used to measure the $\rm H_2$ content of the flowing gas. The gas chromatograph was calibrated at 3 points using calibration bottles with 5, 100, and 1000 ppm of hydrogen in a nitrogen balance. The Faradaic efficiency was calculated using the following equation:

$$\eta_{\text{far}} = \frac{\int_{0}^{t} \frac{C_{\text{H}_2} F_{\text{N}_2}}{10^6 - C_{\text{H}_2}} dt}{\frac{60lt}{2000F}}$$
 (2)

where $C_{\rm H2}$ is the concentration of H_2 measured with CGC 4.0 in ppm, I is the applied current in mA, F is the Faraday constant (96485 C mol⁻¹), and t is total time of the analysis in min.

Solar-driven water electrolysis experiments

Solar-driven water electrolysis was performed using a homebuilt solar simulator with a tungsten–halogen illumination source filtered by a UV filter (Schott GG385) and a daylight filter (Hoya LB120) with intensity adjusted to obtain the operating point current at approx. 1-sun equivalent light intensity. The experiment was done in ambient air, and thus, the tandem solar cell was kept inside a N_2 -filled box and connected to the PEM water electrolysis cell via external cabling. A Keithley 2600 SMU controlled by code written in the LabVIEW environment was used for simultaneous measurement of the current and the voltage across the water electrolysis cell.

Photoluminescence photon flux

Absolute PL measurements were performed in N₂ using an integrating sphere (Avantes, AvaSphere-30-REFL), where a 455 and 850 nm LED light (Thorlabs M455F3-455 fiber coupled LED source) was used to excite the wide- and narrow-bandgap perovskite films or sub-cells in tandem (at ~1 sun equivalent intensity) through an optical fiber fitted with a 550 and 850 nm short pass filter, respectively. The spectra were measured through an optical fiber connected to a calibrated AvaSpec-HERO spectrometer (Avantes) using a 550 and 875 nm long pass filter for the wide- and narrow-bandgap perovskite, respectively.

Film characterization

SEM images were recorded by a FEI Quanta 3D FEG microscopy. A 5-kV electron beam and a secondary electron detector were used. XPS depth profile was measured by a Thermo Scientific K-Alpha with a 180° double-focusing hemispherical analyzer and a 128-channel detector. A monochromatic Al K α radiation was used (1486.6 eV). An argon ion gun with 1000 eV was used to remove the sample layer by layer. One snapshot was taken every 30 s of etching. XRD on perovskite layers was performed using Empyrean, Panalytical with a Cu K α source

(λ = 1.5406 Å). The scan step size was 0.0167°, and the measurements were performed between 5–40°. For XRD and XPS measurements 37.5 mg of solid catalyst were dispersed in 1.159 mL of isopropanol:water 4:1 (v:v). The obtained catalyst inks were then sonicated for at least 10 min before being manually spray-coated using a pneumatic airbrush (Aerotech) at a deposition temperature of 85 °C on cleaned (15 min sonication in acetone and isopropanol, followed by 30 min UV-ozone treatment) glass substrates. The loadings were 1.0 and 0.5 mg cm⁻² for the RuO₂ and Pt catalyst respectively. XRD of the catalysts was recorded using a Bruker 2D phaser with Cu Kα radiation. Measurements were performed in the range 10 – 80° with a step size 0.01° and collection time of 0.2 s. A divergence slit of 0.6 mm and an anti-scatter screen of 0.5 mm were employed.

Reporting summary

Further information on research design is available in the Nature Portfolio Reporting Summary linked to this article.

Data availability

Source data are provided with this paper.

References

- Young, J. L. et al. Direct solar-to-hydrogen conversion via inverted metamorphic multi-junction semiconductor architectures. *Nat. Energy* 2, 17028 (2017).
- Green, M. A. et al. Solar cell efficiency tables (Version 63). Prog. Photovolt. Res. Appl. 32, 3–13 (2024).
- Song, Z. et al. All-Perovskite Tandem Photoelectrodes for Unassisted Solar Hydrogen Production. ACS Energy Lett. 8, 2611–2619 (2023).
- Jiang, Q. et al. Compositional texture engineering for highly stable wide-bandgap perovskite solar cells. Science 378, 1295–1300 (2022).
- Datta, K. et al. Efficient Continuous Light-Driven Electrochemical Water Splitting Enabled by Monolithic Perovskite-Silicon Tandem Photovoltaics. Adv. Mater. Technol. 8, 2201131 (2023).
- Ramadan, A. J., Oliver, R. D. J., Johnston, M. B. & Snaith, H. J. Methylammonium-free wide-bandgap metal halide perovskites for tandem photovoltaics. *Nat. Rev. Mater.* 8, 822–838 (2023).
- Hu, S. et al. Narrow Bandgap Metal Halide Perovskites for All-Perovskite Tandem Photovoltaics. Chem. Rev. 124, 4079–4123 (2024).
- Chen, H. et al. Regulating surface potential maximizes voltage in allperovskite tandems. *Nature* 613, 676–681 (2023).
- Remmerswaal, W. H. M., van Gorkom, B. T., Zhang, D., Wienk, M. M. & Janssen, R. A. J. Quantifying Non-Radiative Recombination in Passivated Wide-Bandgap Metal Halide Perovskites Using Absolute Photoluminescence Spectroscopy. Adv. Energy Mater. 14, 2303664 (2024).
- Liu, C. et al. Bimolecularly passivated interface enables efficient and stable inverted perovskite solar cells. Science 382, 810–815 (2023).
- Hu, S. et al. Optimized carrier extraction at interfaces for 23.6% efficient tin-lead perovskite solar cells. *Energy Environ. Sci.* 15, 2096–2107 (2022).
- Hoke, E. T. et al. Reversible photo-induced trap formation in mixedhalide hybrid perovskites for photovoltaics. *Chem. Sci.* 6, 613–617 (2015).
- Jošt, M., Kegelmann, L., Korte, L. & Albrecht, S. Monolithic Perovskite Tandem Solar Cells: A Review of the Present Status and Advanced Characterization Methods Toward 30% Efficiency. Adv. Energy Mater. 10, 1904102 (2020).
- Roose, B. et al. Electrochemical Impedance Spectroscopy of All-Perovskite Tandem Solar Cells. ACS Energy Lett. 9, 442–453 (2024).

- Lang, F. et al. Proton-Radiation Tolerant All-Perovskite Multijunction Solar Cells. Adv. Energy Mater. 11, 2102246 (2021).
- 16. Thiesbrummel, J. et al. Understanding and Minimizing $V_{\rm OC}$ Losses in All-Perovskite Tandem Photovoltaics. *Adv. Energy Mater.* **13**, 2202674 (2023).
- Hu, S. et al. A Universal Surface Treatment for p-i-n Perovskite Solar Cells. ACS Appl. Mater. Interfaces 14, 56290-56297 (2022).
- Hu, S. et al. Synergistic Surface Modification of Tin-Lead Perovskite Solar Cells. Adv. Mater. 35, 2208320 (2023).
- Wang, J. et al. Halide homogenization for low energy loss in 2-eVbandgap perovskites and increased efficiency in all-perovskite triple-junction solar cells. *Nat. Energy* 9, 70–80 (2024).
- Caprioglio, P. et al. Open-circuit and short-circuit loss management in wide-gap perovskite p-i-n solar cells. *Nat. Commun.* 14, 932 (2023).
- Datta, K. et al. Monolithic All-Perovskite Tandem Solar Cells with Minimized Optical and Energetic Losses. Adv. Mater. 34, 2110053 (2022).
- Moot, T. et al. Choose Your Own Adventure: Fabrication of Monolithic All-Perovskite Tandem Photovoltaics. Adv. Mater. 32, 2003312 (2020).
- Stolterfoht, M. et al. How To Quantify the Efficiency Potential of Neat Perovskite Films: Perovskite Semiconductors with an Implied Efficiency Exceeding 28%. Adv. Mater. 32, 2000080 (2020).
- Fehr, A. M. K. et al. Integrated halide perovskite photoelectrochemical cells with solar-driven water-splitting efficiency of 20.8%. Nat. Commun. 14, 3797 (2023).
- Hansora, D. et al. All-perovskite-based unassisted photoelectrochemical water splitting system for efficient, stable and scalable solar hydrogen production. *Nat. Energy* 9, 272–284 (2024).
- Lyons, M. E. G. & Floquet, S. Mechanism of oxygen reactions at porous oxide electrodes. Part 2—Oxygen evolution at RuO₂, IrO₂ and Ir_xRu_{1-x}O₂ electrodes in aqueous acid and alkaline solution. Phys. Chem. Chem. Phys. 13, 5314–5335 (2011).
- Ma, Z. et al. Reaction mechanism for oxygen evolution on RuO₂, IrO₂, and RuO₂@IrO₂ core-shell nanocatalysts. *J. Electroanal. Chem.* 819, 296–305 (2018).
- Walter, M. G. et al. Solar Water Splitting Cells. Chem. Rev. 110, 6446–6473 (2010).
- 29. Song, S. et al. Electrochemical investigation of electrocatalysts for the oxygen evolution reaction in PEM water electrolyzers. *Int. J. Hydrog. Energy* **33**, 4955–4961 (2008).
- 30. Giordano, L. et al. pH dependence of OER activity of oxides: Current and future perspectives. *Catal. Today* **262**, 2–10 (2016).
- Liu, C. et al. Constructing a Multifunctional Interface between Membrane and Porous Transport Layer for Water Electrolyzers. ACS Appl. Mater. Interfaces 13, 16182–16196 (2021).
- Siracusano, S., Baglio, V., Van Dijk, N., Merlo, L. & Aricò, A. S. Enhanced performance and durability of low catalyst loading PEM water electrolyser based on a short-side chain perfluorosulfonic ionomer. *Appl. Energy* 192, 477–489 (2017).
- Kuang, Y. et al. Solar-driven, highly sustained splitting of seawater into hydrogen and oxygen fuels. *Proc. Natl Acad. Sci.* 116, 6624–6629 (2019).
- Wang, Y. et al. Direct Solar Hydrogen Generation at 20% Efficiency Using Low-Cost Materials. Adv. Energy Mater. 11, 2101053 (2021).
- Park, H. et al. Water Splitting Exceeding 17% Solar-to-Hydrogen Conversion Efficiency Using Solution-Processed Ni-Based Electrocatalysts and Perovskite/Si Tandem Solar Cell. ACS Appl. Mater. Interfaces 11, 33835–33843 (2019).
- Luo, J. et al. Water photolysis at 12.3% efficiency via perovskite photovoltaics and Earth-abundant catalysts. Science 345, 1593–1596 (2014).

- 37. Jošt, M. et al. Subcell Operation and Long-Term Stability Analysis of Perovskite-Based Tandem Solar Cells Using a Bichromatic Light Emitting Diode Light Source. Sol. RRL 5, 2100311 (2021).
- Al-Ashouri, A. et al. Monolithic perovskite/silicon tandem solar cell with >29% efficiency by enhanced hole extraction. Science 370, 1300–1309 (2020).
- Knight, A. J., Patel, J. B., Snaith, H. J., Johnston, M. B. & Herz, L. M. Trap States, Electric Fields, and Phase Segregation in Mixed-Halide Perovskite Photovoltaic Devices. *Adv. Energy Mater.* 10, 1903488 (2020).
- 40. Mahesh, S. et al. Revealing the origin of voltage loss in mixed-halide perovskite solar cells. *Energy Environ*. Sci. **13**, 258–267 (2020).
- 41. Datta, K. et al. Effect of Light-Induced Halide Segregation on the Performance of Mixed-Halide Perovskite Solar Cells. ACS Appl. Energy Mater. 4, 6650–6658 (2021).
- 42. Lin, Y. H. et al. A piperidinium salt stabilizes efficient metal-halide perovskite solar cells. Science **369**, 96–102 (2020).
- Werner, J. et al. Improving Low-Bandgap Tin-Lead Perovskite Solar Cells via Contact Engineering and Gas Quench Processing. ACS Energy Lett. 5, 1215–1223 (2020).
- 44. Chen, B. et al. Bifacial all-perovskite tandem solar cells. Sci. Adv. 8, eadd0377 (2022).
- Prasanna, R. et al. Design of low bandgap tin-lead halide perovskite solar cells to achieve thermal, atmospheric and operational stability. Nat. Energy 4, 939–947 (2019).
- 46. Siekmann, J. et al. Characterizing the Influence of Charge Extraction Layers on the Performance of Triple-Cation Perovskite Solar Cells. *Adv. Energy Mater.* **13**, 2300448 (2023).
- 47. Fu, S. et al. Suppressed deprotonation enables a durable buried interface in tin-lead perovskite for all-perovskite tandem solar cells. *Joule* **8**, 2220–2237 (2024).
- 48. Tan, S. et al. Sustainable thermal regulation improves stability and efficiency in all-perovskite tandem solar cells. *Nat. Commun.* **15**, 4136 (2024).
- Tong, J. et al. Carrier lifetimes of >1 μs in Sn-Pb perovskites enable efficient all-perovskite tandem solar cells. Science 364, 475–479 (2019).
- 50. Lin, R. et al. Monolithic all-perovskite tandem solar cells with 24.8% efficiency exploiting comproportionation to suppress Sn(II) oxidation in precursor ink. *Nat. Energy* **4**, 864–873 (2019).
- 51. Wang, J. et al. 16.8% Monolithic all-perovskite triple-junction solar cells via a universal two-step solution process. *Nat. Commun.* 11, 5254 (2020).

Acknowledgements

This work was supported by the European Union's Horizon Europe research and innovation programme under grant agreement numbers 101075605 (SuPerTandem) and 101075330 (NEXUS). We further acknowledge funding from the Dutch Research Council (NWO, Spinoza grant) and the European Union (ERC, PERSTACK, 101098168). N.R.M.S. acknowledges funding from HyET Solar Netherlands B.V. J.W. and H.J.S. acknowledge the UKRI for guarantee funding for Marie Skłodowska-Curie Actions (MSCA) Postdoctoral Fellowships award (SEALPTSC, EP/Y029216/1). A.W. acknowledges the New Energy and Industrial Technology Development Organization (NEDO) and JST Mirai (JPMJMI22E2). We also acknowledge Solliance, a partnership of R&D organizations from The Netherlands, Belgium and Germany working in thin-film photovoltaic solar energy.

Author contributions

J.W., B.B., M.M.W., and R.A.J.J. planned the research and performed the analysis. J.W., B.B., and V.Z. fabricated the tandem solar cells. B.B. developed the water electrolysis experiments and performed the subcell *J–V* analysis. W.H.M.R. performed the intensity-dependent PLQY

measurements and analyzed the results. S.H. prepared the Sn-Pb films for aging tests and investigated the cross-sectional morphology using SEM. A.W. provided FTO substrates for wide-bandgap solar cell experiments. N.R.M.S. helped optimizing the wide-bandgap single-junction solar cells. L.B. performed the XPS and XRD measurements and analysis. N.D. assisted with electrochemical analysis. J.W., B.B., and R.A.J.J. composed the initial draft, and all authors commented on it. H.J.S. and R.A.J.J. secured the funding and facilitated the equipment for characterization. H.J.S. and R.A.J.J. supervised the project.

Competing interests

H.J.S. is cofounder and CSO of Oxford PV Ltd. A.W. is co-founder and CSO of Enecoat Technologies Co., Ltd. All other authors declare no competing interests.

Additional information

Supplementary information The online version contains supplementary material available at https://doi.org/10.1038/s41467-024-55654-4.

Correspondence and requests for materials should be addressed to René A. J. Janssen.

Peer review information *Nature Communications* thanks Jinlong Gong, Jae Sung Lee, and the other, anonymous, reviewer(s) for their contribution to the peer review of this work. A peer review file is available.

Reprints and permissions information is available at http://www.nature.com/reprints

Publisher's note Springer Nature remains neutral with regard to jurisdictional claims in published maps and institutional affiliations.

Open Access This article is licensed under a Creative Commons Attribution-NonCommercial-NoDerivatives 4.0 International License, which permits any non-commercial use, sharing, distribution and reproduction in any medium or format, as long as you give appropriate credit to the original author(s) and the source, provide a link to the Creative Commons licence, and indicate if you modified the licensed material. You do not have permission under this licence to share adapted material derived from this article or parts of it. The images or other third party material in this article are included in the article's Creative Commons licence, unless indicated otherwise in a credit line to the material. If material is not included in the article's Creative Commons licence and your intended use is not permitted by statutory regulation or exceeds the permitted use, you will need to obtain permission directly from the copyright holder. To view a copy of this licence, visit https://creativecommons.org/licenses/by-nc-nd/4.0/.

© The Author(s) 2024